PAPER

Aerodynamic effects of varying solid surface area of bristled wings performing clap and fling

To cite this article: Mitchell P Ford et al 2019 Bioinspir. Biomim. 14 046003

View the article online for updates and enhancements.



IOP ebooks™

Bringing you innovative digital publishing with leading voices to create your essential collection of books in STEM research.

Start exploring the collection - download the first chapter of every title for free.

Bioinspiration & Biomimetics



RECEIVED
4 January 2019

REVISED

2 April 2019

ACCEPTED FOR PUBLICATION 16 April 2019

PUBLISHED 17 May 2019

PAPER

Aerodynamic effects of varying solid surface area of bristled wings performing clap and fling

Mitchell P Ford¹, Vishwa T Kasoju¹, Manikantam G Gaddam¹ and Arvind Santhanakrishnan^{1,2}®

- ¹ School of Mechanical and Aerospace Engineering, Oklahoma State University, Stillwater, OK 74078, United States of America
- ² Author to whom any correspondence should be addressed.

E-mail: askrish@okstate.edu

Keywords: thrips, fairyflies, bristled wings, flapping flight, clap and fling, aerodynamics Supplementary material for this article is available online

Abstract

The smallest flying insects with body lengths under 2 mm show a marked preference for wings consisting of a thin membrane with long bristles, and the use of clap and fling kinematics to augment lift at Reynolds numbers (Re) of approximately 10. Bristled wings have been shown to reduce drag forces in clap and fling, but the aerodynamic roles of several bristled wing geometric variables remain unclear. This study examines the effects of varying the ratio of membrane area $(A_{\rm M})$ to total wing area $(A_{\rm T})$ on aerodynamic forces and flow structures generated during clap and fling at Re on the order of 10. We also examine the aerodynamic consequences of scaling bristled wings to Re = 120, relevant to flight of fruit flies. We analyzed published forewing images of 25 species of thrips (Thysanoptera) and found that $A_{\rm M}/A_{\rm T}$ ranged from 14% to 27%, as compared to 11% to 88% previously reported for smaller-sized fairyflies (Hymenoptera). These data were used to develop physical bristled wing models with $A_{\rm M}/A_{\rm T}$ ranging from 15% to 100%, which were tested in a dynamically scaled robotic clap and fling model. At all Re, bristled wings produced slightly lower lift coefficients (C_1) when compared to solid wings, but provided significant drag reduction. At Re = 10, largest values of peak lift over peak drag ratios were generated by wing models with $A_{\rm M}/A_{\rm T}$ similar to thrips forewings (15% to 30%). Circulation of the leading edge vortex and trailing edge vortex decreased with decreasing $A_{\rm M}/A_{\rm T}$ during clap and fling at Re =10. Decreased chordwise circulation near the wing tip, vortex shedding, and interaction between flow structures from clap with those from fling resulted in lowering C_L generated via clap and fling at Re = 120 as compared to Re = 10. Clap and fling becomes less beneficial at Re = 120, regardless of the drag reduction provided by bristled wings.

Introduction

Despite an extreme reduction in size by over two orders of magnitude from larger insects such as hawkmoths, honey bees, and dragonflies, flight capability is retained among thousands of species of tiny insects with body lengths ranging from 0.2 to 2 mm. Thysanoptera (thrips) alone accounts for eight different families of tiny insects containing more than 5500 known species (Morse and Hoddle 2006). In addition to thrips, Mymaridae (fairyflies) and Trichogrammatidae constitute two different Hymenopteran families of tiny Chalcid wasps, representing several hundred more species of tiny flying insects. Collectively, these insects are often studied for their agricultural and ecological importance, both as biological vectors of

plant pathogens (Ullman *et al* 2002, Jones 2005) and for applications in biological control (Austin and Dowton 2000). However, details of their lifecycles, dispersal mechanisms, and wing design remain largely unclear (Mound 2005, Jones *et al* 2016). Given that the smallest insects are also among the smallest metazoans (Polilov 2015, Sane 2016), studies of flapping flight of tiny insects can offer insight into size constraints of flapping as a biological locomotion strategy.

Tiny flying insects operate at wing-chord based Reynolds number (Re) on the orders of 1 to 10, where viscous effects are significant (Miller and Peskin 2004, Santhanakrishnan *et al* 2014). Santhanakrishnan *et al* (2018) found that at Re below 30, dimensionless lift coefficients of a revolving elliptical wing increase slightly compared to higher Re, but dimensionless drag

coefficients increase by several hundred percent. Overcoming this increased drag force, which is due to the large viscous dissipation of kinetic energy at low Re, places significant energetic demands on these insects as they must flap continuously in order to stay aloft (Sane 2016). Tiny insects have evolved several biomechanical adaptations to overcome this challenge. Specifically, the use of 'clap and fling' wingbeat kinematics (Weis-Fogh 1973) has been observed in tiny insects such as Encarsia formosa (Weis-Fogh 1973), Muscidifurax raptor and Nasonia vitripennis (Miller and Peskin 2009). During the clap phase, the wings come in close proximity to each other at the end of the upstroke. This is followed by the fling phase at the start of the downstroke, where the wings rotate about their trailing edges and translate away from each other. The clap and fling kinematics allows each wing to operate near or at maximum stroke amplitude, and has been shown to provide aerodynamic benefits via: 1) generating bound circulation at the leading edges of the wings during fling with little to no circulation at the trailing edges, conducive for lift generation (Weis-Fogh 1973, Lighthill 1973, Bennett 1977, Ellington 1984, Miller and Peskin 2005); and 2) generating downward flow during clap that can be used to generate additional thrust for maneuvering (Ellington 1984, Ellington et al 1996). Though the use of clap and fling is also seen in larger insects such as tethered butterflies and Drosophila, observations of the obligate use of this mechanism have been limited strictly to the smallest insects (Lehmann et al 2005). Several computational studies (Miller and Peskin 2005, Kolomenskiy et al 2011, Arora et al 2014) have shown that more lift enhancement via clap and fling is observed in the range of low Re relevant to tiny insect flight, as compared to larger Re where viscous forces are much lower (e.g. inviscid clap and fling considered by Lighthill (1973)).

Though clap and fling can provide lift enhancement, there is a large drag penalty associated with the fling of a wing pair at low Re on the order of 10 (Miller and Peskin 2005, Kasoju et al 2018). Due to the presence of bristled wings in most, if not all, species of tiny insects capable of free flight, they have been conjectured to serve a unique function in helping overcome the challenges of flapping flight at low Re. Weis-Fogh (1973) originally suggested that bristles could help prevent the wings from sticking together. Single wing studies have since shown only minimal force reduction of bristled wings when compared to solid wings (Sunada et al 2002, Lee and Kim 2017). However, computational studies of clap and fling at low Re have shown that bristled wings can provide substantial drag reduction when compared to solid wings (Santhanakrishnan et al 2014, Jones et al 2016). In a recent experimental study, Kasoju et al (2018) found that flow leaking through the bristles contributed to the observed drag reduction during clap and fling of bristled wings. This study also reported that bristled wings reduced

drag by a larger extent than lift when compared to solid wings.

Despite a number of recent studies examining aerodynamic performance of bristled wings, the roles of individual bristled wing design variables have been largely unaddressed. Bristled wing design studies have thus far been limited to examining how altering the gap between bristles affects aerodynamic performance (Jones et al 2016, Lee and Kim 2017, Kasoju et al 2018). Computational studies of interacting bristled wings are challenging due to the difficulty in needing to simultaneously resolve flow around individual bristles (order of 1 micron) as well as flow around the wings (order of 1 mm). Santhanakrishnan et al (2014) performed 2D clap and fling computations and modeled bristled wings as porous plates. Jones et al (2016) addressed some of the morphological diversity of wing design in Mymaridae, but only examined the fluid dynamic effects of the ratio of gap width to bristle diameter, where the wing was modeled using a row of 2D cylinders. The relative importance of a number of geometric variables of bristled wing design on aerodynamic force generation remain unclear, including: area of the solid membrane relative to total wing area, number of bristles per unit span, angle of bristles relative to the membrane, and the relative lengths of bristles on either side of the wing.

The specific aim of this study is to examine how variations to the solid membrane area of bristled wings affects the aerodynamic forces and flow structures generated during clap and fling. The total wing area (A_T) and membrane area (A_M) were measured in several species of thrips (order: Thysanoptera), and the percentage of the wing covered by the membrane (A_M/A_T) was calculated and compared to data presented for fairyflies (order: Hymenoptera, family: Mymaridae) reported in Jones et al (2016). Thysanoptera proved ideal for this study, as the Mymaridae species examined by Jones et al (2016) had body lengths ranging from 0.17-1.0 mm, while the Thysanoptera species in this study had body lengths ranging from 0.9-1.8 mm. Together, the two datasets contain the whole known range of flying 'tiny' insects, from the smallest fairyflies up to the largest thrips, and should provide important insight into the constraints underlying the design of bristled wings. The morphological data from the two studies were used to design biomimetic physical models of bristled wings, which were tested on a robotic platform performing clap and fling. We also examined scalability of bristled wings interacting via clap and fling at Re larger than the order of 10 that is relevant to the flapping flight of tiny insects.

Materials and methods

This study examines previously published images of the forewings of several species of thrips (Order: Thysanoptera) to quantify: body length, solid membrane area ($A_{\rm M}$), total wing area ($A_{\rm T}$), and area occupied by bristles ($A_{\rm B}$). The ratio of the solid membrane area to the total wing area ($A_{\rm M}/A_{\rm T}$) was used to develop physical models, which were then tested on a robotic platform designed to mimic clap and fling kinematics used in previous studies (Miller and Peskin 2005, Miller and Peskin 2009, Arora *et al* 2014, Kasoju *et al* 2018). Strain gauge measurements were acquired to quantify dimensionless lift and drag forces generated during clap and fling, and 2D particle image velocimetry (PIV) measurements were performed to visualize the flow generated along the wing chord at different spanwise planes and quantify circulation of leading and trailing edge vortices.

Bristled wing morphology

Morphological data were collected from previously published images of 25 species of Thysanoptera from a total of three different taxonomic families in order to determine the range of variation in biological wing design, especially the ratio of solid membrane area to the total wing area (Funderburk et al 2007, Mound and Ng 2009, de Borbón 2010, Riley et al 2011, Cavalleri and Mound 2012, Minaei and Aleosfoor 2013, Tong et al 2015, Lima and Mound 2016). Thrips were chosen for this study especially due to their size and lack of close taxonomic relations with other tiny insects such as Mymaridae, which have previously been studied by Jones et al (2016). Jones et al (2016) examined 23 species of fairyflies (Hymenoptera: Mymaridae), and found correlations with body length in the ratio of gap spacing between bristles to bristle diameter, and in the percentage of wing area occupied by bristles $(A_{\rm B})$. However, Jones et al (2016) found a strong negative correlation between bristled area (AB) and body length, and suggested that (in fairyflies) bristled wings should be uncommon in insects larger than 1 mm in body length (Jones et al 2016). Adult thrips often have body lengths measuring 1 mm to 2 mm, and are larger than smaller insects in Mymaridae and Trichogrammatidae. Due to their larger size and weight, thrips would comparatively require more control and larger lift forces in free flight. Therefore, studies of the wing design and flight mechanics in thrips could provide unique insights into bristled wing design.

In this study, we considered only images that clearly showed at least one forewing with all the bristles and no visible sign of damage to the wing. Morphometric analyses were performed on these images using ImageJ software (Schneider *et al* 2012), and membrane area ($A_{\rm M}$) and total wing area ($A_{\rm T}$) were directly measured from the images (figure 1(A)). Bristled wing area ($A_{\rm B}$) was calculated as the difference between $A_{\rm T}$ and $A_{\rm M}$. The percentage of the wing covered by the membrane relative to total wing area ($A_{\rm M}/A_{\rm T}$) was used in physical model design, rather than $A_{\rm B}/A_{\rm T}$, as $A_{\rm M}$ was directly measured whereas $A_{\rm B}$ was calculated. The values of $A_{\rm M}$, $A_{\rm T}$, $A_{\rm B}$, and $A_{\rm M}/A_{\rm T}$ were plotted as functions

of body length (figures 1(B)–(D)). Linear regressions were performed in each case, and R^2 and P-values were reported for each regression. A full list of species and measurements is provided as supplementary material (table S1 (stacks.iop.org/BB/14/046003/mmedia)).

Wing models

Based on the morphological data from the order Thysanoptera (this study) and family Mymaridae (Jones et al 2016), 5 pairs of bristled wings covering the range of A_M/A_T values found in both families of tiny insects were designed in SolidWorks software (Dassault Systèmes SE, Vélizy-Villacoublay, France). The selected $A_{\rm M}/A_{\rm T}$ values for this study were $A_{\rm M}/A_{\rm T} = 15\%$, $A_{\rm M}/A_{\rm T} = 30\%$, $A_{\rm M}/A_{\rm T} = 50\%$, $A_{\rm M}/A_{\rm T}=70\%$, and $A_{\rm M}/A_{\rm T}=100\%$ (a completely solid wing). A_T was maintained constant across all bristled wing models, and $A_{\rm M}$ was varied to achieve the desired $A_{\rm M}/A_{\rm T}$. Physical models of bristled wing pairs and a solid wing pair were experimentally tested on a robotic model mimicking clap and fling kinematics (figures 2(B), (C), 3(A) and (B)). The idealized wing models were constructed in-house, with solid membranes laser cut from 1.5 mm thick polycarbonate sheets, and bristles cut to desired lengths from commercially available 1 mm diameter borosilicate glass rods. Clear epoxy was used to bond the polycarbonate membranes to either side of the glass bristles. These materials were chosen because they were optically clear for flow visualization using particle image velocimetry (PIV).

Total wing area (A_T) , gap to diameter ratio (G/D), number of bristles, angle of bristles relative to the centerline of the wing, and aspect ratio (AR, defined as the ratio of wing span to average chord length) were maintained constant across the five bristled wing models in order to ensure that any effects found in the study would be strictly due to the change in relative membrane area. The solid wing model had an identical total wing area and AR as all the bristled wing models. The inter-bristle gap (G) to bristle diameter (D) ratio (G/D)was maintained constant at 8 across all bristled wing models, which is within the biological range observed in thrips and in fairyflies (Jones et al 2016). The number of bristles was limited to 20 in all bristled wing models, due to the 1 mm minimum diameter of commercial borosilicate glass rods (used to mimic bristles) while being constrained to be within a biologically relevant *G/D* ratio. The number of bristles seen on the forewings of thrips (~50-120) was not achievable and is noted as a limitation of this study. However, smaller insects such as fairyflies typically have between 20-35 bristles. Angle of the bristles relative to the wing was maintained constant at 45° in all bristled wing models. There is a wide range of variation in the angle of bristles in thrips and fairyflies, and many species of thrips have been reported to adjust the angle of their bristles for flight (Mound 2005). Additionally, a non-bristled wing model, identical in geometry to the membrane of the $A_{\rm M}/A_{\rm T}=70\%$ model was constructed and strain

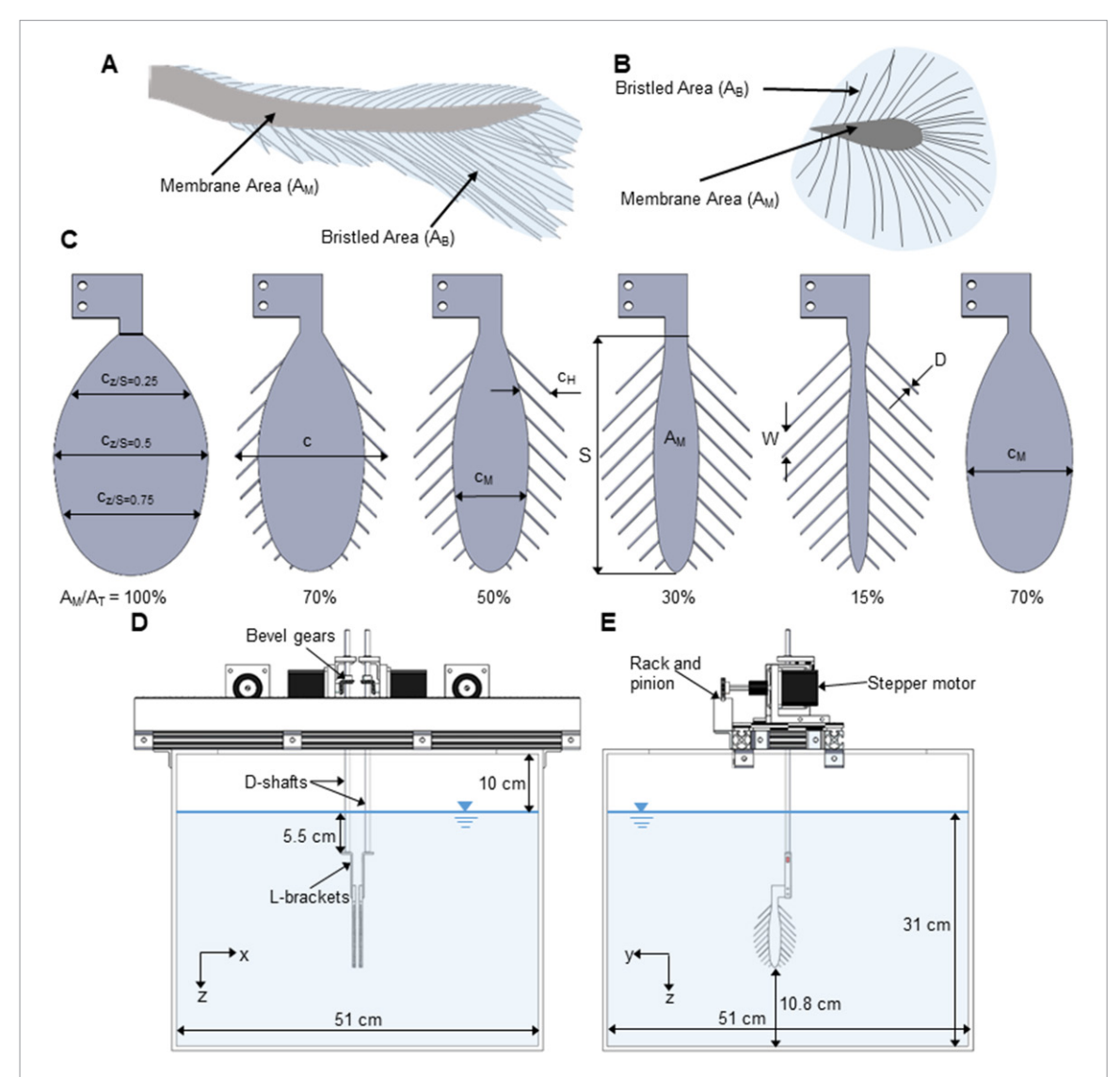


Figure 1. Wing models and robotic platform used in this study. (A) Forewing of *Thrips setosus* (body length: 1250–1330 μ m) is shown in top, redrawn from Riley et al (2011), with both A_B and A_M indicated. (B) For contrast, the forewing of fairyfly Mymar sp. (body length: 589–1024 μ m) with lower number of bristles is shown in bottom, redrawn from Lin et al (2007). ImageJ software (Schneider et al 2012) was used to measure A_M and A_T , while A_B was calculated as: $A_B = A_T - A_M$. (C) Bristled wing models with ratios of membrane area to total area of (left to right): $A_M/A_T = 100\%$ (solid), $A_M/A_T = 70\%$, $A_M/A_T = 50\%$, $A_M/A_T = 30\%$, $A_M/A_T = 15\%$, where A_M is the membrane area and A_T is the total wing area. The membrane only model shown on the far right has the same A_M as in the model with $A_M/A_T = 70\%$, but with the bristles excluded. Chord lengths (c) at varying locations on the wing span are indicated as $c_{z/S}$, and representative labels are shown for $c_{z/S=0.25}$, $c_{z/S=0.75}$. Portions of the chord covered by the solid membrane and by the bristles are denoted and shown as c_M and c_H , respectively. The parameter of specific interest to this study, A_M/A_T , was varied by changing the length of c_M relative to c, while maintaining a constant span (S) of 90 mm and average chord of 45 mm. Across all bristled wing models, gap width (G) of 8 mm was maintained as a constant, and bristle diameter (D) of 1 mm was maintained as a constant. The total number of bristles on each bristled wing was maintained constant at n = 20. Figures (D) and (D) indicate front and right side views, respectively, of the robotic model used in this study. Stepper motors, rack and pinion mechanism, bevel gears, and D-shafts used to drive a pair of physical wing models are shown, along with distances from the wing models to the tank walls and to the free surface of the fluid. The coordinate system used throughout this paper is also shown.

gauge data were collected. This model is referred to as the 'membrane only' wing, and was used to isolate the effects of adding bristles on aerodynamic forces (by comparing with $A_{\rm M}/A_{\rm T}=70\%$ bristled wing model). It is important to note that since the membranes for each bristled wing were made by reducing chord length relative to the solid wing, the membrane only wing had a higher AR than the solid and bristled wings. The AR (ratio of span length to average chord length) for the solid wing models and all bristled wing models is 2. The AR of the membrane only wing is 2.86, which is similar to AR = 2.91 of *Drosophila* (Harbig *et al* 2013).

Robotic model

The dynamically scaled robotic model used in this study (figures 2(B) and (C)) was the same platform used in Kasoju *et al* (2018), and was experimentally validated in the aforementioned study against Sunada *et al* (2002) for a single wing in translation at varying angles of attack. Wing models were attached to 6.35 mm diameter stainless steel *D*-shafts via custom made aluminum *L*-brackets. Each wing was driven by two 2-phase hybrid stepper motors with integrated encoders (ST234E, National Instruments Corporation, Austin, TX, USA). One stepper motor

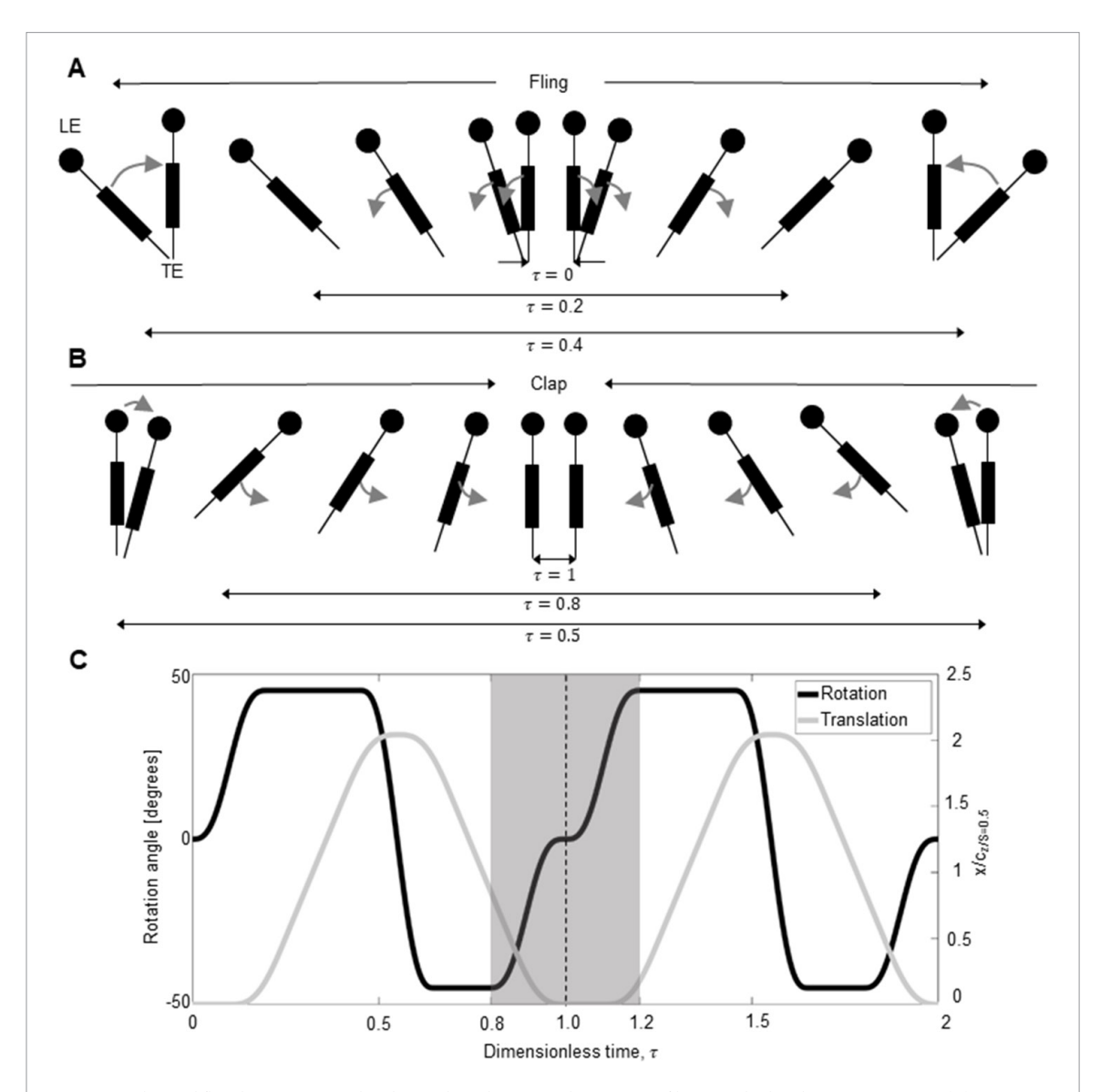


Figure 2. Clap and fling kinematics used in this study and associated motion profile prescribed to the stepper motors. (A) Matchstick diagram depicting fling kinematics in the x-y plane, where the wing chord is shown as it would appear along a cut-section along the span. Time points are nondimensionalized as: $\tau = t/T$, where T denotes the overall stroke period (values of T are in table 1). $\tau = 0$, $\tau = 0.2$, and $\tau = 0.4$ represent the start of rotation, end of rotation, and the start of the stroke reversal, respectively. Leading and trailing edges of the model are marked as LE and TE, respectively. (B) Matchstick diagram depicting the clap portion of the stroke. $\tau = 0.5$, $\tau = 0.8$, and $\tau = 1$ represent the end of the stroke reversal, the start of rotation, and the end of both rotation and translation. (C) Time-varying motion profile prescribed to the stepper motors for a single wing, developed based on a previous study by Miller and Peskin (2005). Left hand side y-axis shows the rotation angle of a wing, plotted as a thick solid line. Right hand side y-axis shows wing translation distance, plotted as a thin solid line (along the x-coordinate in (B)) non-dimensionalized by chord length along mid-span of the wing. The shaded region from $\tau = 0.8$ to $\tau = 1.2$ represents the clap and fling portion of the stroke where strain gauge and PIV data were acquired. Data acquisition was performed from the end of one cycle (clap) to the beginning of the next cycle (fling). A 50% overlap between rotation and translation was prescribed during fling, and a 100% overlap between rotation and translation was prescribed to the motors controlling the left and right wings were identical in magnitude but opposite in sign, so that the wings would travel in opposite directions.

on each side of the platform was connected to a *D*-profile shaft via bevel gears and used for wing rotation. A second stepper motor on each side of the platform used a rack and pinion mechanism to provide wing translation. All four stepper motors were controlled by a multi-axis controller (PCI-7350, National Instruments Corporation, Austin, TX, USA) via custom programs in written in LabVIEW software (National Instruments Corporation, Austin, TX, USA). The motion profiles prescribed to the motors controlling the left and right wings were identical in magnitude but opposite in sign, so that the wings

would travel in opposite directions. The starting distance between the wings was set to 10% of chord at half-span ($c_{z/S=0.5}$) for all experiments used in this study. This distance is similar to those observed in previous high-speed video recordings of freely flying thrips (Santhanakrishnan *et al* 2014), and is close enough to experience wing—wing interactions, but just far enough apart to prevent the leading and trailing edges of the rigid wing models from colliding during rotation. The assembly was mounted on an acrylic tank with a square base measuring 0.51 m on each side, and 0.41 m in height. The tank was filled to

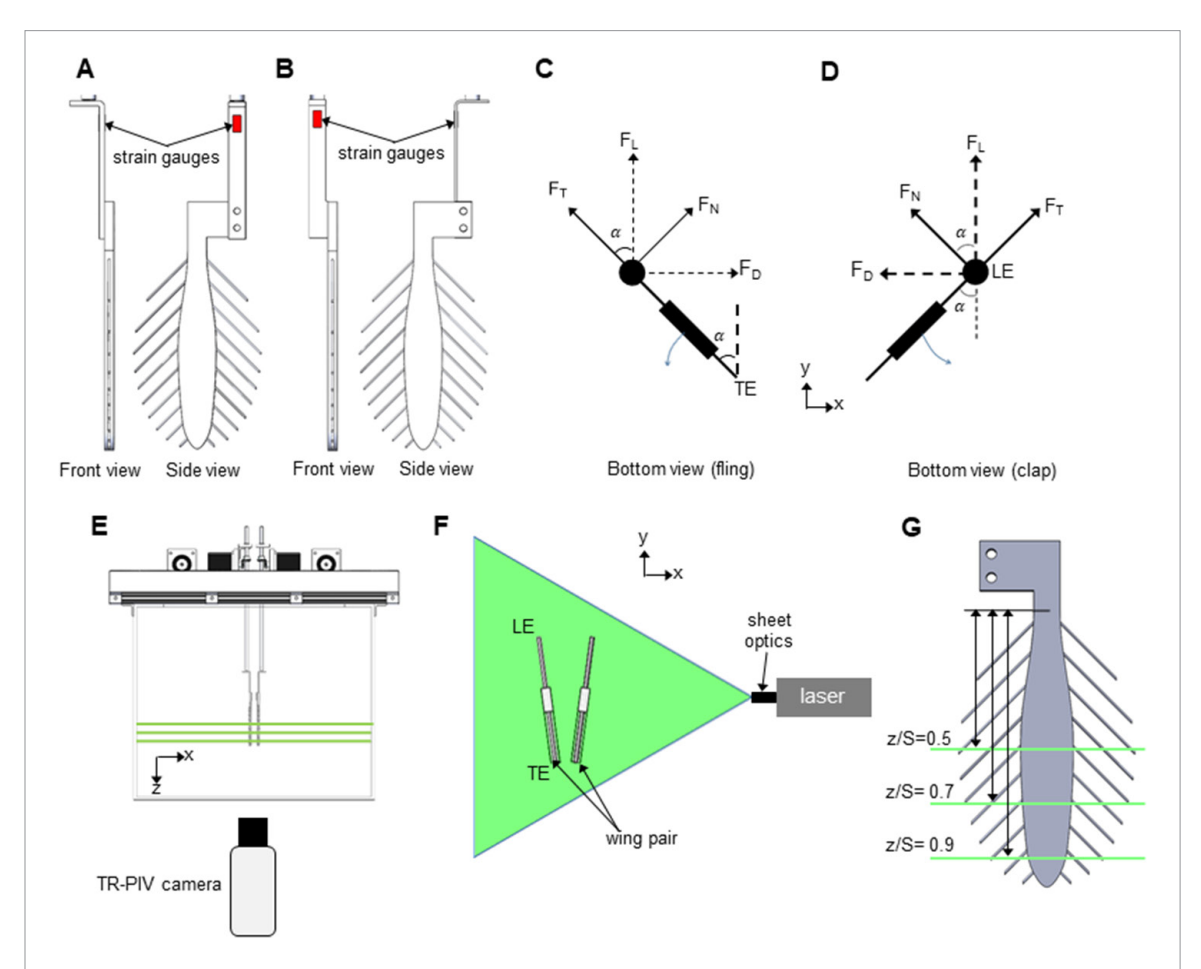


Figure 3. Diagrams showing force measurement setup with strain gauges and experimental setup used for PIV measurements. (A) Front and side views of a representative wing model mounted onto a custom L-bracket configured for drag data collection. (B) Front and side views of a representative wing model mounted onto a custom L-bracket configured for lift data collection. (C) and (D) Normal force $(F_{\rm N})$, tangential force $(F_{\rm T})$, lift force $(F_{\rm L})$, and drag force $(F_{\rm D})$ definitions shown on a representative wing during fling (C) and clap (D) phases. The wing in (C) and (D) is shown in the chordwise x-y plane looking above from the bottom of the tank (i.e. looking above from the bottom of figure 2(A)). (E) PIV setup with high-speed camera, with the three different laser planes at spanwise locations of z/S = 0.5 (50% span), z/S = 0.7 (70% span), and z/S = 0.9 (90% span) indicated. (F) Camera view of wings during PIV data acquisition, with laser sheet and coordinate system used for data analysis indicated. (G) Positions of chordwise laser planes at z/S = 0.5; z/S = 0.7; and z/S = 0.9 used in PIV measurements shown along the span of a representative wing.

Table 1. Experimental conditions examined in this study. Each row contains information pertaining to the conditions at a specific Reynolds number (Re) based on the chord length of the solid wing. Each Re shown in column 1 was calculated from equation (2) using the kinematic viscosity (ν) and steady translational velocity (U_{ST}) in columns 3 and 4, respectively. Cutoff frequencies used in the filtering of raw voltage data recorded by lift and drag strain gauges (f_{cutoff}) were varied with U_{ST} , and are shown in column 5. The total length of the rotation part of clap and fling (where strain gauge and 2D time-resolved particle image velocimetry (TR-PIV) data were collected) and the overall stroke period (T) are presented in columns 6 and 7, respectively. 2D TR-PIV camera recording rates are shown in column 8.

Re	Density (kg m ⁻³)	Kinematic viscosity (mm ² s ⁻¹)	$U_{\rm ST}$ (m s ⁻¹)	f_{cutoff} (Hz)	Clap/fling duration (ms)	T (ms)	TR-PIV frame rate (frames s ⁻¹)
10	1215	860	0.19	24	820	2060	244
60	1234	142	0.19	24	820	2060	244
120	1260	72	0.19	24	820	2060	244

0.31 m in height with glycerin-water solutions of varying viscosities (values in table 1), which were used to achieve desired Reynolds numbers while maintaining the same motion profile.

Kinematics

The robotic model is controlled via a custom program using LabVIEW software (National Instruments Corporation, Austin, TX, USA) using kinematics identical to those in a recent experimental study on clap and fling (Kasoju *et al* 2018), and are a slightly

modified version of the 2D clap and fling motion profile used in several previous studies (Miller and Peskin 2005, Arora et al 2014, Santhanakrishnan et al 2014, Jones et al 2016). Angular and translational positions of the wings in time were prescribed to the stepper motors (figure 3(C)). There was 100% overlap prescribed between rotation and translation during clap, meaning that the wings were translating toward each other during the entire time that they were rotating. A 50% overlap between rotation and translation was prescribed during fling, so that each

wing of the wing pair had rotated 22.5° (half of total 45° rotation) before translation began. Arora et al (2014) previously examined the effects of varying the percentage overlap between rotation and translation on forces generated during clap and fling. Diagrams showing the kinematics used in this study for fling (figure 3(A)) and clap (figure 3(B)) indicate the direction of motion and wing position at the start and end of each portion of the stroke. Aerodynamic forces generated by clap and fling of 2D solid wings using these kinematics have been well characterized for varying Re, wing spacing, and percentage overlap for translation and rotational motion (Miller and Peskin 2005, Arora et al 2014). Further, biological observations of clap and fling in freely flying tiny insects (Weis-Fogh 1973, Ellington 1984) are often qualitative, due to lack of control of animal position and orientation when acquiring camera footage at high magnification and frame rates.

For the motion profile used in this study, displacement is reported in chord lengths, rotation angle is reported in degrees, and a dimensionless time was defined as

$$\tau = t/T,\tag{1}$$

where t represents the amount of time elapsed since the start of wing motion, while T represents the length of one complete wingbeat cycle. Therefore, τ can be considered physically the number of wingbeat cycles elapsed since the start of motion.

Test conditions

Each wing model used in this study was tested at three different Re ranging from Re = 10 to Re = 120. The Reynolds number (Re) of a fluid flow is defined as the ratio of inertial forces to viscous forces, and was calculated in this study as

$$Re = \frac{c \cdot U_{ST}}{\nu}, \qquad (2)$$

where c is average chord length across the span of the forewing, U_{ST} is wing tip velocity during steady translation, and ν is the kinematic viscosity of the fluid medium. Note that the characteristic velocity in this equation is the steady-state velocity during wing translation, which allows Re to be calculated as a single value across the entire stroke, rather than as a time-varying parameter. This definition has been used in a number of previous studies relevant to tiny insect flight (Sunada et al 2002, Miller and Peskin 2005, Santhanakrishnan et al 2014, Jones et al 2016, Kasoju et al 2018). Since chord length and motion profile were constant for all wing models, Re was varied only by changing fluid viscosity. To achieve the three different Re tested in this study, three different glycerin-water solutions were made with varying viscosities (table 1). This method of varying kinematic viscosity has been used previously to achieve a wide range of Re without having to change wing models or velocity (Maxworthy

1979). For the different fluid mixtures, kinematic viscosities were measured using Cannon-Fenske routine viscometers of sizes 200, 300, and 400 (Cannon Instrument Company, State College, PA, USA). The duration of the clap and fling portion of the stroke, T, was a function of the motion profile and $U_{\rm ST}$, with clap and fling taking the same length of time, T/2.

Force measurements

Force data were collected by means of strain gauges bonded to the L-brackets shown in (figures 4(A) and (B)) using the robotic platform shown in (figures 2(B) and (C)). A data acquisition board (NI USB-6210, National Instruments Corporation, Austin, TX, USA) sampled the raw voltage data, while the same LabVIEW (National Instruments Corporation, Austin, TX, USA) program used to control the motors triggered the recording of strain gauge data and angular position of the wings at a sample rate of 100 kHz throughout the duration of clap and fling wing-wing interaction ($\tau = 0.8$ –1.2). The sampling and processing procedures were the same as used in Kasoju et al (2018), with voltage signal being recorded prior to the start of motion for a baseline offset. Ten consecutive motion profile cycles (totaling 20 stroke periods or wingbeat cycles) were run prior to data collection in order to establish a periodic steady state in the tank, and voltage data were recorded for the next 30 continuous cycles. Raw voltage data were processed in MATLAB (The Mathworks Inc., Natick, MA, USA) using a simulated third order low-pass Butterworth filter with the cutoff frequencies given in (table 1). The cutoff frequency for filtering voltage data (f_{cutoff}) was a function of U_{ST} , as in Kasoju et al (2018), and was maintained constant across wing models for a specific Re. The filtered baseline offset was subtracted from the filtered voltage data, and the results were used to calculate forces on the strain gauge brackets via manual calibration of the lift and drag brackets. Then, lift and drag forces acting on the wings were calculated as tangential force in the positive y-direction, and normal force in the x-direction, respectively (figures 4(C) and (D)). These were calculated according to equations (3) and (4):

$$F_{\rm L} = F_{\rm T} {\rm cos} \alpha \tag{3}$$

$$F_{\rm D} = F_{\rm N} {\rm cos} \alpha,$$
 (4)

where $F_{\rm T}$ and $F_{\rm N}$ are tangential and normal forces as defined in (figures 4(C) and (D)), and α is the rotation angle of the wing, as recorded from the integrated encoder in the rotation stepper motor. Inertial forces were recorded for wing pair motion with the tank being empty and were subtracted from the filtered lift and drag data prior to calculation of dimensionless lift ($C_{\rm L}$) and drag ($C_{\rm D}$) coefficients. $C_{\rm L}$ and $C_{\rm D}$ were calculated as

$$C_{\rm L} = \frac{L}{\frac{1}{2}\rho U_{\rm ST}^2 A_{\rm T}},\tag{5}$$

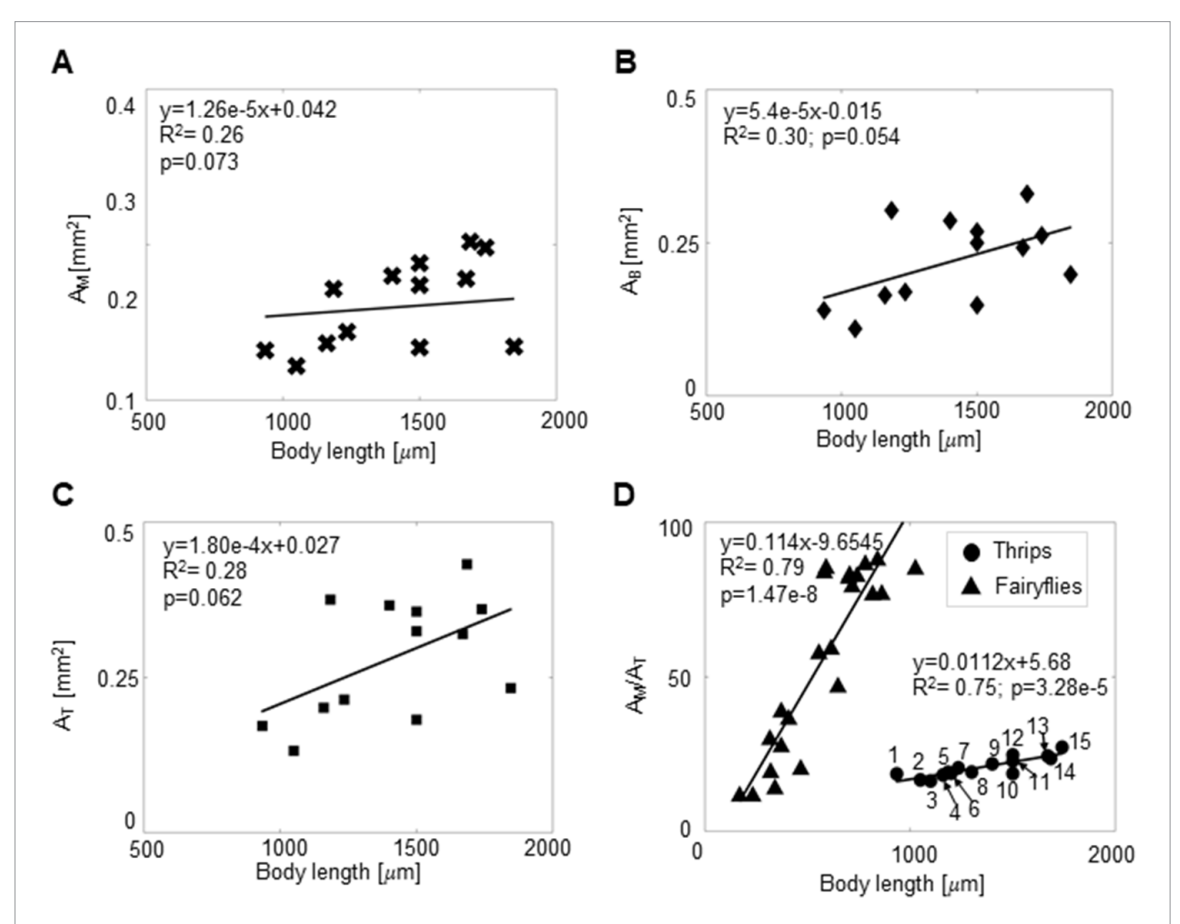


Figure 4. Morphological data obtained from published images of Thysanoptera forewings. (A) Measured values of $A_{\rm M}$ as a function of body length. (B) Measured values of $A_{\rm T}$ as a function of body length. (C) Calculated values of $A_{\rm B}$ as a function of body length. (D) Ratio of membrane area to total wing area, $A_{\rm M}/A_{\rm T}$, as a function of body length in Thysanoptera (measured in this study) and in Mymaridae (from Jones et al (2016)). Linear regressions for each data set are shown with R^2 and p-values. Species numbered in (D): (1) Scirtothrips dorsalis (Riley et al 2011) (2) Lenkothrips mollinediae (Cavalleri and Mound 2014) (3) Chaetanaphothrips orchidi (Funderburk et al 2007) (4) Neohydatothrips ikelus (Lima and Mound 2016) (5) Neohydatothrips chelinus (Lima and Mound 2016) (6) Neohydatothrips sidae (Lima and Mound 2016) (7) Ceratothripoides claratris (Riley et al 2011) (8) Neohydatothrips hemileucus (Lima and Mound 2016) (9) Thrips setosus (Riley et al 2011) (10) Thrips tabaci (Riley et al 2011) (11) Frankliniella gemina (Riley et al 2011) (12) Heterothrips pilarae (de Borbón 2010) (13) Frankliniella schultzei (Riley et al 2011) (14) Frankliniella occidentalis (Riley et al 2011) (15) Frankliniella intonsa (Riley et al 2011). The full list of all Thysanoptera species examined in this study and measurements is provided as supplementary material (table S1).

$$C_{\rm D} = \frac{D}{\frac{1}{2}\rho U_{\rm ST}^2 A_{\rm T}},$$
 (6)

where L and D are the lift and drag forces, respectively, in Newtons, and ρ is density of the fluid medium. Standard deviations were calculated across all cycles for C_L and C_D , and the force coefficients were averaged across 30 cycles. The strain gauges used to collect force data were mounted on the L-brackets attaching the wings to the robotic platform, and recorded per-wing force rather than overall force. For this reason, lift and drag coefficients presented throughout this paper are presented in terms of dimensionless force per wing.

Particle image velocimetry

2D time-resolved particle image velocimetry (TR-PIV) measurements were acquired for each wing model in three different chordwise planes (parallel to the *x-y* plane) located at $c_{z/S=0.5}$ (50% span), $c_{z/S=0.7}$ (70% span), and $c_{z/S=0.9}$ (90% span) as shown in figures 4(E)–(G). The TR-PIV setup used in this study was similar to the one described in Kasoju

et al (2018), but with a 50 mm Nikon AF Nikkor lens (model number 1902, Nikon Corporation, Tokyo, Japan) in order to acquire a wider field of view. Image capture was performed using LaVision DaVis 8.3.0 software (LaVision GmbH, Göttingen, Germany). Hollow glass spheres of 10 μ m diameter were used as seeding particles (110P8, LaVision GmbH, Göttingen, Germany), and a homogeneous initial distribution of particles was verified prior to running the model for each PIV trial. A Nd:YLF single cavity diode pumped solid state laser (527 nm wavelength) with 1kHz maximum repetition rate and 0.5 mm beam diameter was used as the illumination source (Photonics Industries International, Inc., Bohemia, NY, USA). The beam was passed through a divergingconverging lens combination and a horizontal laser sheet of 2-3 mm in thickness was developed using a 10 mm focal-length cylindrical lens. A high speed CMOS camera with a spatial resolution of 1280×800 pixels, maximum frame rate of 1630 frames s⁻¹, and pixel size of 20 microns × 20 microns (Phantom Miro 110, Vision Research Inc., Wayne, NJ, USA) was

mounted on a rail below the tank, and was triggered to capture 200 images using a high speed controller (model number 1108075, LaVision GmbH, Göttingen, Germany). PIV image acquisition was triggered via the same LabVIEW program that was used to control the wing motion (National Instruments Corporation, Austin, TX, USA). The frame rate required to capture 100 evenly spaced images each during clap and fling was calculated based on $U_{\rm ST}$ for a specific Re (table 1).

Cross-correlation of raw PIV images was performed in DaVis 8.3.0 software (LaVision GmbH, Göttingen, Germany) in multiple passes of decreasing size, with one pass using an interrogation window size 48×48 pixels, and two subsequent passes using window sizes of 24×24 pixels. PIV results were averaged over ten cycles, and positions and 2D velocity vector fields were exported. Vorticity was used to quantify fluid rotation around the wing, calculated from the velocity field data as

$$\omega_z = \frac{\partial v}{\partial x} - \frac{\partial u}{\partial y},\tag{7}$$

where ν represents local velocity in the y direction, and u represents local velocity in the x direction. Circulations of leading and trailing edge vortices were calculated from the vorticity fields at 11 time points each for clap and fling, taken at time steps of 5% of stroke period T. Circulation was calculated using a custom MATLAB script (The Mathworks Inc., Natick, MA, USA), and the values of circulation are presented as a function of τ in (figure 9). Circulation was calculated using the following equation:

$$\Gamma = \iint \omega_z dS, \qquad (8)$$

where *S* is the vorticity region for either the leading edge or trailing edge vortex. Circulation values for select cases and a diagram showing how the box containing the vortex was drawn are provided in the supplementary information (figure S3). A high-pass vorticity cutoff was used to isolate the core of each vortex. The cutoff value was set to 25% of the maximum vorticity magnitude in each vortex (LEV cutoff = $0.25 * \omega_{z,max,LEV}$, TEV cutoff = $0.25 * \omega_{z,max,TEV}$), and was calculated separately for clap and for fling using the wing model with $A_{\rm M}/A_{\rm T}=15\%$ (the smallest membrane area). Other cutoff values, ranging from 5% to 20% of the maximum vorticity, were examined for the solid and bristled wing models with $A_{\rm M}/A_{\rm T}=15\%$ at Re = 10. 25% cutoff was found to provide consistently repeatable results between different users. Also, varying cutoff percentage resulted in small changes to the values of LEV and TEV circulation during clap phase and even smaller changes during fling phase (figure S3). The timevariation of circulation was unaffected by the choice of cutoff value, as long as a cutoff was used. Note that circulation in this study is presented for the right wing only, with the assumption that circulations of leading and trailing edge vortices generated around the left wing will be equivalent in magnitude but oppositely signed. Finally, though the rotational directions of the LEV and TEV are reversed in clap and fling, we present LEV circulation as positive values and TEV circulation as negative values (in both clap and fling) to facilitate comparison between each half-stroke.

Results and discussion

Wing morphology

This study examined the forewing morphology in 25 species of tiny free-flying insects called thrips (order Thysanoptera), and compared the ratios of solid membrane area relative to total wing area to those of even smaller fairyflies (family Mymaridae) that were previously reported by Jones et al (2016). For thrips, total wing area (A_T) and solid membrane area (A_M) were measured and recorded along with the body length of the specimen. The area occupied by bristles in thrips' forewings (A_B) was calculated by taking the difference of the total wing area and solid membrane area $(A_{\rm M}-A_{\rm T})$. Weak positive correlations were found between $A_{\rm M}$, $A_{\rm B}$, $A_{\rm T}$, and body length (BL), with R^2 values of 0.30, 0.26, and 0.28, and p-values of 0.054, 0.073, and 0.062, respectively (n = 13, figures 4(A) -(C)).

The dimensionless ratio of solid membrane area to total wing area (A_M/A_T) was determined in 15 species of thrips and plotted against body length, and a strong positive correlation was found, with $R^2 = 0.75$ and $p = 3.28 \times 10^{-5}$ (figure 4(D)). Previously, Jones et al (2016) had found a strong positive correlation between A_M/A_T and body length in fairyflies $(R^2 = 0.79, p = 1.47 \times 10^{-8}, n = 23)$. A number of images of thrips forewings available in the literature were suitable for determining $A_{\rm M}/A_{\rm T}$, but did not report body lengths of the specimens. $A_{\rm M}/A_{\rm T}$ for these species is reported in the supplementary information (table S1), and in each case falls well within the range of $A_{\rm M}/A_{\rm T}$ values included in the regressions in figure 4(D). The value of $A_{\rm M}/A_{\rm T}$ in all 25 different species of thrips fell into a relatively tight range of 14%-27%. This contrasts sharply with the $A_{\rm M}/A_{\rm T}$ range of 11%–88% reported for 23 species of fairyflies by Jones et al (2016).

Based on extrapolation of the $A_{\rm M}/A_{\rm T}$ data in fairy-flies, one would expect thrips to present with solid wings ($A_{\rm M}/A_{\rm T}=100\%$) rather than bristled wings. Similar extrapolation of the data obtained from thrips would predict $A_{\rm M}/A_{\rm T}$ in fairyflies to fall mostly between 10%-15%, or only about 1/15th of the total range of $A_{\rm M}/A_{\rm T}$ values that were actually present in fairyflies. From previous studies (Santhanakrishnan *et al* 2014, Jones *et al* 2016, Kasoju *et al* 2018), it is clear that bristled wings have aerodynamic benefits. However, the importance of the majority of bristled wing geometric design variables on clap and fling aerodynamics remains unclear. The relatively tight distribution of

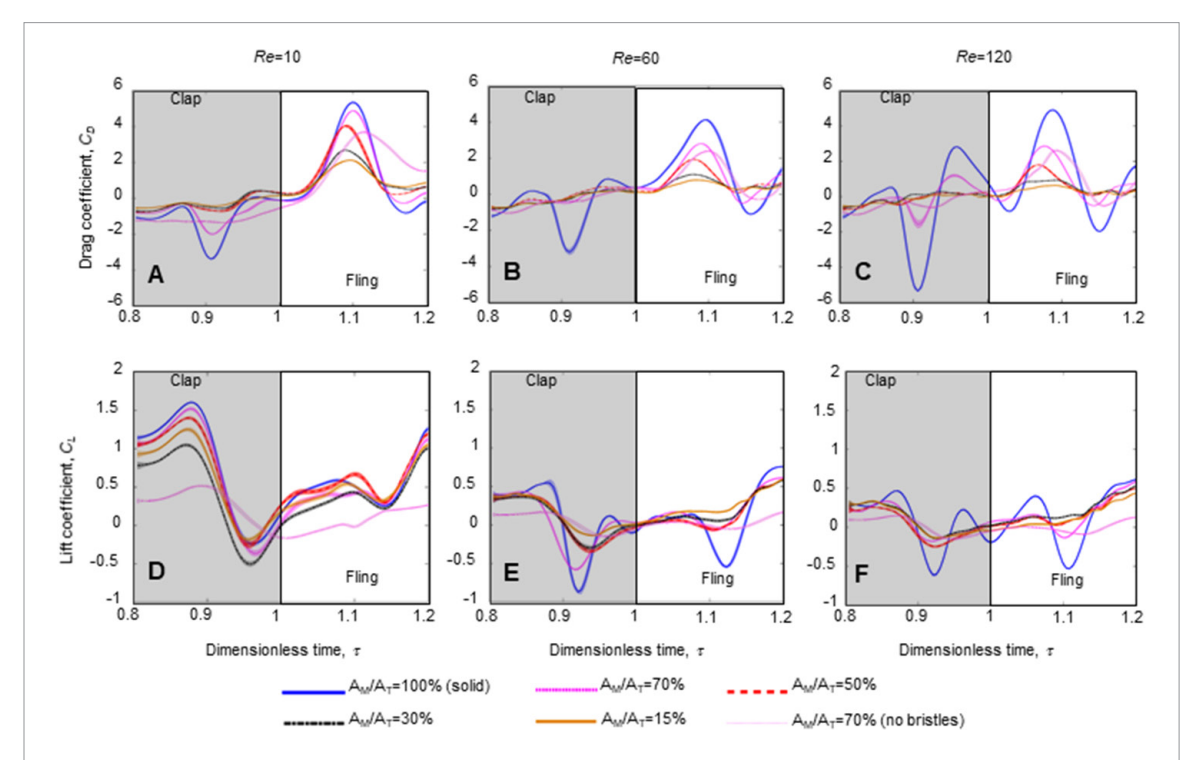


Figure 5. Time variation of drag coefficient C_D and lift coefficient C_L . (A)–(C) Drag coefficients at Re = 10, 60, and 120. (D)–(F) Lift coefficients at Re = 10, 60, and 120. As Re increases from 10 to 120, more fluctuation can be seen in drag coefficients over cycle time, while lift coefficients are reduced during both clap and fling. In the case of drag coefficient, the membrane only wing $(A_M/A_T = 70\%$ with no bristles) performs similarly to the bristled wings, but is seen to generate much lower lift forces. This is consistent with larger effective wing spacing (distance between wings divided by chord) and with lower aspect ratio (Harbig *et al* 2013, Arora *et al* 2014).

 $A_{\rm M}/A_{\rm T}$ ranging from 14%–27% in thrips (figure 4(D)) may potentially be of functional relevance, i.e. the $A_{\rm M}/A_{\rm T}$ range where improved aerodynamic efficiency (lift over drag ratio) of bristled wings in clap and fling may be realized. However, the larger range of $A_{\rm M}/A_{\rm T}$ of fairyflies suggests that clap and fling aerodynamic performance may not be the sole driver behind this trait in at least one order of tiny insects. The rationale behind physical model experiments discussed in the following sections was to evaluate how varying $A_{\rm M}/A_{\rm T}$ impacts aerodynamic force generation in clap and fling to identify if there is, in fact, a preferred range of $A_{\rm M}/A_{\rm T}$ that would augment aerodynamic efficiency.

Aerodynamic forces in clap and fling

At low Re relevant to the flight of the smallest insects, overcoming drag becomes more difficult than generating lift (Santhanakrishnan et al 2018). Santhanakrishnan et al (2014), Jones et al (2016) and Kasoju et al (2018) found that bristled (or porous) wings can greatly reduce the drag force experienced during the fling portion of the stroke, while maintaining much of the lift force. Kasoju et al (2018) showed that leaked flow through inter-bristle gaps, characterized using leakiness proposed by Cheer and Koehl (1987), was the mechanism underlying this drag reduction. This study examined aerodynamic force generation under varying A_M/A_T in bristled wings performing clap and fling, as well as under varying Re from 10 to 120. The goal of this study was to determine whether there is an optimal $A_{\rm M}/A_{\rm T}$ for bristled wings

performing clap and fling at Re = 10 based on lift over drag ratio, and whether this optimal value remains unchanged as Re increases by an order of magnitude from 10 to 120.

Force measurements were taken at three different Re (10, 60, and 120) ranging from the Re of tiny insects (Re = 10) to that of fruit flies (Re = 120), with lift and drag forces defined as force generated by the prescribed motion of a wing in the vertical and horizontal directions (independent of local wing angle), respectively. The time-resolved dimensionless forces (figure 5) were found to follow the same general trend as seen in previous clap and fling studies using solid wings (Miller and Peskin 2005, Miller and Peskin 2009, Arora et al 2014) and bristled or porous wings (Santhanakrishnan et al 2014, Jones et al 2016, Kasoju et al 2018). However, the maximum values of the force coefficients were lower in this study, likely due to the elliptical planform of the wing models used here (chord length varied along the span of the wing), since previous studies have modeled wings as infinitely long rectangles (2D representation) or having a rectangular planform (3D representation).

The negative peak seen in $C_{\rm D}$ during clap (figures $5({\rm A})$ –(C)) indicates drag acting in the opposite direction during clap as compared to during fling. The peak value of the drag coefficient, $C_{\rm D,max,clap}$, occurs just over halfway through the clap, at approximately $\tau=0.91$. This coincides with the rotational deceleration of the wing (figure $3({\rm C})$). The maximum drag coefficient during fling, $C_{\rm D,max,fling}$, was found to occur approximately halfway through the fling, at $\tau=1.1$ (figures

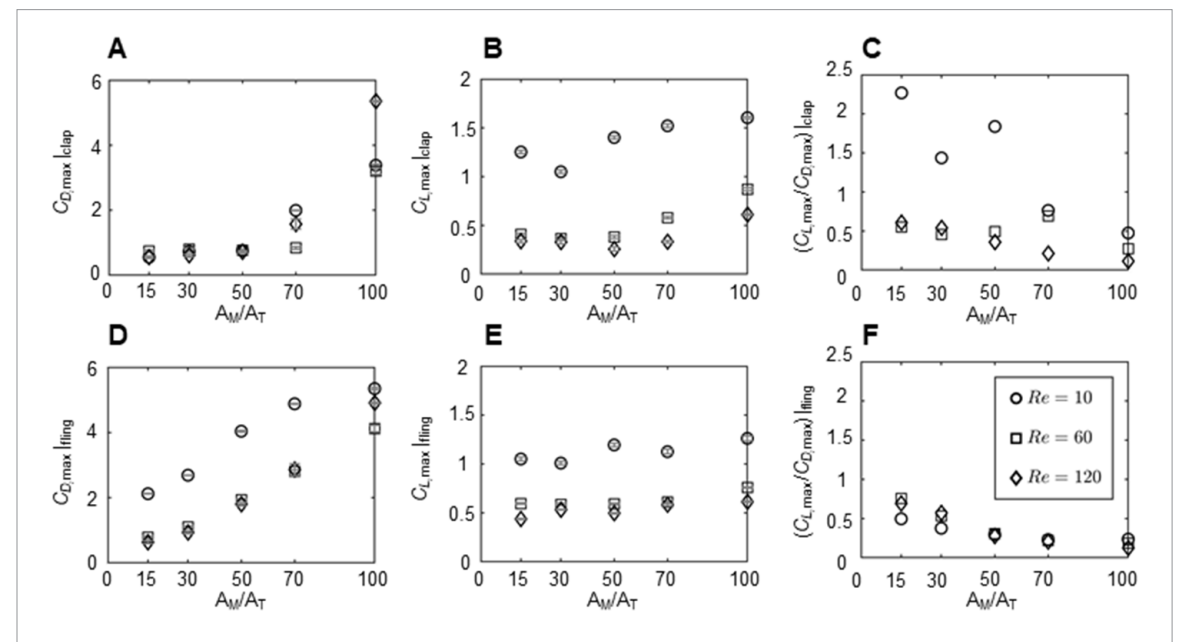


Figure 6. Peak lift and drag coefficients during clap and fling as a function of Reynolds number and A_M/A_T . Top (A)-(C): peak values of drag coefficients, lift coefficients, and the ratio of peak lift to peak drag during clap. Bottom (D)-(F): peak values of drag coefficients, lift coefficients, and the ratio of peak lift to peak drag during fling. Decreasing A_M/A_T results in lower drag coefficients, while lift is maintained. Decreasing Re results in higher lift coefficients, as well as higher drag coefficients in fling.

5(A)–(C)). This time point corresponds to the rotational deceleration of the wing, as well as the start of translational motion (figure 3(C)). Local maxima were found in C_L during clap ($\tau \approx 0.86$), before the start of rotational deceleration, as well as at the end of fling ($\tau = 1.2$), which coincides with the start of the downstroke (figure 5). Both C_L and C_D generally decreased with decreasing A_M/A_T in both clap and fling.

In general, increasing Re resulted in larger fluctuations to both $C_{\rm L}$ and $C_{\rm D}$ throughout the duration of the cycle (figure 5). Also as Re increased, the maximum values of $C_{\rm L}$ and $C_{\rm D}$ were reduced, with the greatest reduction in $C_{\rm L}$ occurring during clap (compare figures 6(B) and (E)), and the greatest reduction in $C_{\rm D}$ occurring during fling (compare figures 6(A) and (D)). This change results in maximal lift occurring during clap for Re = 10, and at the end of fling for both Re = 60 and Re = 120 (figure 5), meaning that tiny insects benefit more from the clap than larger insects. Peak dimensionless force values are discussed more thoroughly in the next section.

In addition to the five different bristled wing models, data were also collected on a 'membrane only' model, which was equivalent in geometry to the $A_{\rm M}/A_{\rm T}=70$ wing without bristles. This model showed $C_{\rm D}$ similar to the $A_{\rm M}/A_{\rm T}=70\%$ wing model, but showed $C_{\rm L}$ much lower than all the bristled wing models, and a lift to drag ratio slightly lower than that of the solid wing (figures 5 and S1). The peak dimensionless lift in clap at Re = 10 for $A_{\rm M}/A_{\rm T}=70\%$ wing model with bristles (figure 5, $C_{\rm L,max,clap}=1.52$) was nearly three times of $A_{\rm M}/A_{\rm T}=70\%$ wing model without bristles (figure 5, $C_{\rm L,max,clap}=0.52$). In short, the membrane only wing provided no benefits when compared to the solid wing, and performed much worse

than the equivalent bristled wing. This agrees with the computational results of Harbig et al (2013) of a modified Drosophila wing, which showed that higher aspect ratio wings can be detrimental to lift generation, and with Arora et al (2014) which showed that increasing the dimensionless gap length between the wings (gap divided by chord length) can cause a reduction in aerodynamic forces. Though the gap length was unchanged in both $A_{\rm M}/A_{\rm T}=70\%$ wing models that were tested (with and without bristles), the chord length of the $A_{\rm M}/A_{\rm T}=70\%$ wing model without bristles was smaller. This rendered the non-dimensional gap length (inversely related to chord) larger for the $A_{\rm M}/A_{\rm T} = 70\%$ wing model without bristles, which showed a large reduction in lift coefficients in clap and fling at all three values of Re that were examined in this study. Overall, these results demonstrate that the area occupied by the bristles contribute to lift generation by densely bristled wings like those seen in most tiny insects, rather than only the solid membrane. This is likely due to interaction of shear layers formed on closely-spaced adjacent bristles, as discussed in Kasoju et al (2018).

Effects of wing design and Reynolds number on peak dimensionless forces

The maximum values of $C_{\rm L}$ and $C_{\rm D}$, as well at the ratio $C_{\rm L}/C_{\rm D}$ were plotted as functions of $A_{\rm M}/A_{\rm T}$, with different marker styles representing different Reynolds numbers (figure 6). $C_{\rm D,max}$ was found to increase monotonically with increasing $A_{\rm M}/A_{\rm T}$ during fling, but remained almost constant for $A_{\rm M}/A_{\rm T}$ between 15%–50% during clap, before increasing as $A_{\rm M}/A_{\rm T}$ increased from 50%–100%. As Re changed from Re = 60 to Re = 120, there was little change in $C_{\rm D,max}$,

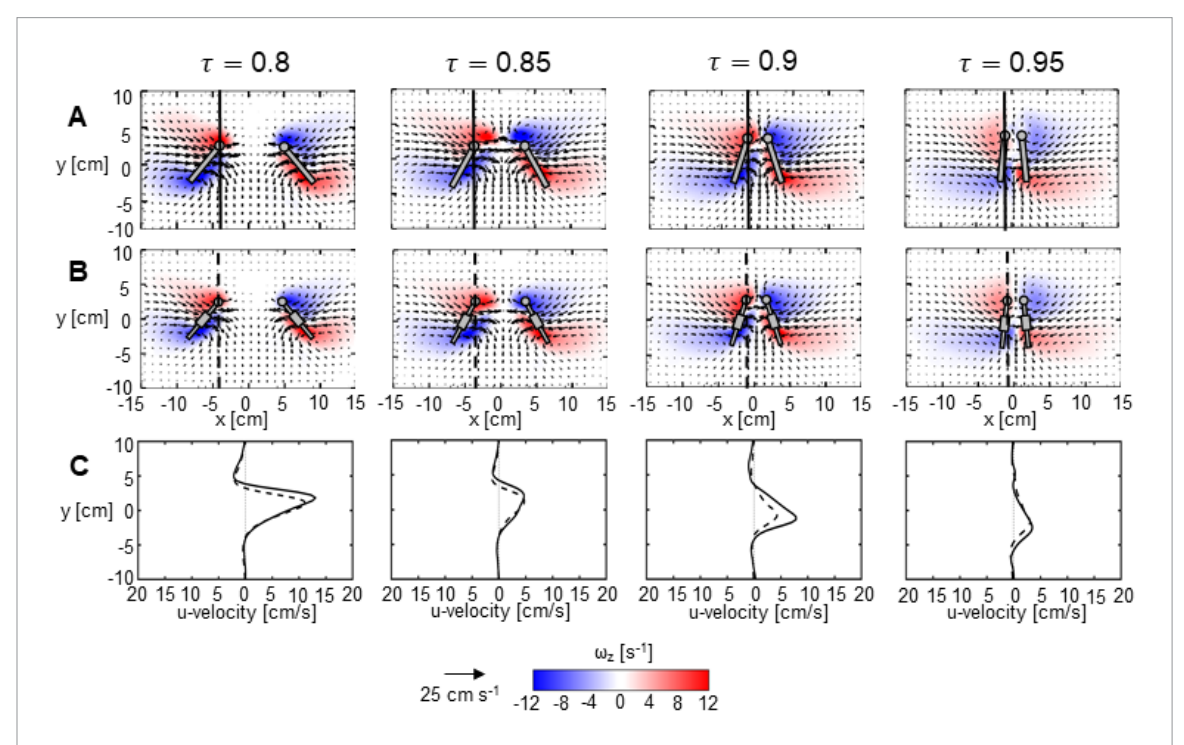


Figure 7. Velocity vector fields overlaid with out-of-plane (z) vorticity contours in the chordwise plane at z/S=0.5 and Re = 10. (A) Solid wing pair during clap. (B) Bristled wing pair of $A_{\rm M}/A_{\rm T}=15\%$ during clap. (C) x-velocity at the leading edge of the wing. The solid black line indicates x-velocity induced by the solid wing, while the dashed line indicates x-velocity induced by the bristled wing. Columns 1, 2, 3, and 4 indicate 0%, 25%, 50%, and 75% of clap. In terms of τ , columns 1 through 4 correspond to $\tau=0.8$ (column 1), 0.85 (column 2), 0.9 (column 3), 0.95 (column 4). The wing position has been superimposed on each image, and a filled circle represents the leading edge of each wing. Reference vectors and vorticity contours are the same across all images. Indicated wing sizes are approximately to scale. Bristled wings show smaller vorticity regions than solid wings at any particular time point. Previous studies (Jones *et al* 2016, Kasoju *et al* 2018) have associated the decreased vorticity and velocity generated by bristled wings in fling at Re = 10 with reduction in drag coefficients due to leaky inter-bristle flow, while lift is reduced to a smaller extent.

especially for values of $A_{\rm M}/A_{\rm T}$ below 50% (figures 6(A) and (D)). However, as Re decreased from Re = 60 to Re = 10, $C_{\rm D,max}$ greatly increased (see figure 5(E) for example).

As with $C_{D,max}$, $C_{L,max}$ showed little change between Re = 60 and Re = 120, especially when compared with the change between Re = 10 and Re = 60 (figures 6(B) and (E)). Unlike $C_{D,max}$, however, $C_{L,max}$ remained largely unaffected with increasing A_{M}/A_{D} , and the result is that bristled wings preserve the vast majority of the lift force achieved by solid wings, while cutting down on the drag force. (Percent reduction in $C_{D,max}$, and in $C_{L,max}$ of bristled wings compared to solid wings are presented in the supplementary figure S1.). The rise in force coefficients at low Re relevant to the flight of tiny insects agrees with the findings of Miller and Peskin (2005).

The lift to drag ratio is a commonly used measure of aerodynamic efficiency, which in the biological case compares the amount of force exerted that contributes to keeping the insect aloft to the amount of force required just to move the wings through the fluid medium (air). The ratio of peak lift to peak drag is shown in (figures 6(C) and (F)). Solid wings performed the worst in terms of peak lift to peak drag ratio, $C_{L,max}/C_{D,max}$, across all Reynolds numbers, with bristled wings showing elevated values of $C_{L,max}/C_{D,max}$ due to large drag reduction without loss of lift. $C_{L,max}/C_{D,max}$ decreased with increasing A_M/A_T values

during both clap and fling, meaning that the smaller the membrane, the more aerodynamically efficient the wing when performing clap and fling. This occurred at all Re, but the benefit to bristled wings in terms of $C_{\rm L,max}/C_{\rm D,max}$ was most pronounced at Re = 10. Reductions in $A_{\rm M}/A_{\rm T}$ resulted in higher ratios of peak lift to peak drag in this study, but with little drag benefit in clap to having wings with $A_{\rm M}/A_{\rm T}$ below 50%, and diminishing returns for reducing $A_{\rm M}/A_{\rm T}$ below 30% in fling. This makes bristled wings with $A_{\rm M}/A_{\rm T}$ of 15% to 30% the most aerodynamically efficient, which is close to the range of $A_{\rm M}/A_{\rm T}$ of 14% to 27% observed in thrips (figure 4(D)).

Flow in the chordwise plane due to clap and fling

Velocity vector fields were obtained from 2D TR-PIV data in three horizontal planes located at 50%, 70%, and 90% span, measured from wing root to wing tip (supplementary videos 1–3). Acquiring PIV data in these planes allows for observation of how chordwise flow changes along the span with increasing Reynolds number. Plots showing velocity fields overlaid on vorticity contours are presented here for the mid-span (z/S = 50%) at 8 select time points for $A_{\rm M}/A_{\rm T} = 15\%$ and $A_{\rm M}/A_{\rm T} = 100\%$ and Re = 10 (figures 7 and 8). Horizontal velocity profiles were extracted along a vertical line drawn from the leading edge of the left wing at the same time points, to show how the flow changes in time (figures 7(C) and 8(C)).

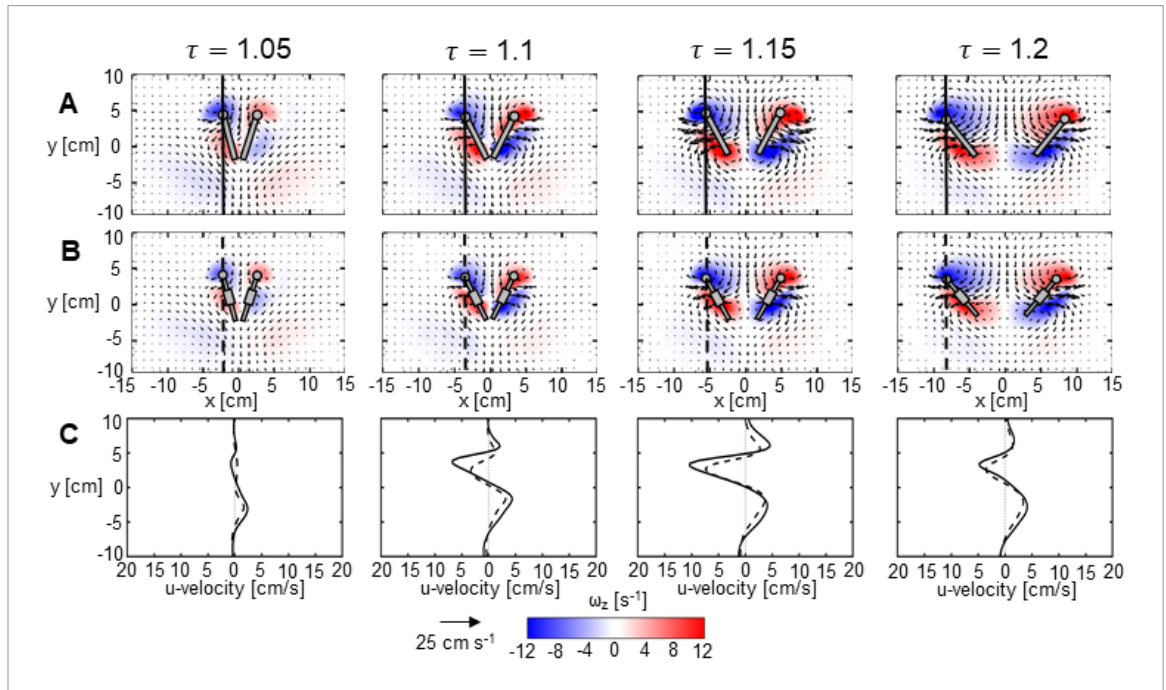


Figure 8. Velocity vector fields overlaid with out-of-plane (z) vorticity contours in the chordwise plane at z/S=0.5 and Re =10. (A) Solid wing pair during fling. (B) Bristled wing pair of $A_{\rm M}/A_{\rm T}=15\%$ during fling. (C) x-velocity at the leading edge of the wing. The solid black line indicates x-velocity induced by the solid wing, while the dashed line indicates x-velocity induced by the bristled wing. Columns 1, 2, 3, and 4 indicate 25%, 50%, 75%, and 100% of fling. In terms of τ , columns 1 through 4 correspond to $\tau=1.05$ (column 1), 1.1 (column 2), 1.15 (column 3), and 1.2 (column 4).

Both the leading (LEV) and trailing (TEV) vortices initially grow stronger during clap at Re = 10 as flow from the two wings begins to interact and wing rotation begins (figure 7(A)). These vortices then dissipate towards the end of clap as translational and rotational velocity slow (figure 7(A)). Velocity in the horizontal direction was shown at $\tau = 0.825, 0.875,$ 0.925, and 0.975 (figure 7(C)). These profiles show that velocity at the leading edge of the most bristled wing $(A_{\rm M}/A_{\rm T}=15\%)$ closely tracks with the velocity at the leading edge of the solid wing, except at $\tau = 0.925$, where the horizontal velocity of the flow caused by the bristled wing is much lower than that caused by the solid wing (figure 7(C)). This difference in horizontal velocity occurs at the same time as the maximum drag force observed during clap, which was dramatically reduced for bristled wings with $A_{\rm M}/A_{\rm T} < 70\%$ (figures 5(A)-(C) and 6(A).

During fling at Re = 10 (figure 8), both the LEV and TEV enlarge as time progresses from $\tau=1.025$ to 1.175, with a small region of high vorticity developing between $\tau=1.025$ and 1.075, during rotational acceleration of the wing, and then enlarging without increasing the vorticity in the vortex core between $\tau=1.075$ and 1.175 (figure 8(A)). Initially, there is little difference between horizontal velocity generated by the motion of the bristled versus the solid wing, but once the core of the leading edge vortex is developed by $\tau=1.075$, the horizontal velocity of the fluid pushed by the solid wing is clearly greater, with the bristled wing velocity then slowly catching up with that of the solid wing between $\tau=1.075$ and 1.175 (figure 8(C)). Since the horizontal velocity caused by the bristled and solid wings are

close to the same after $\tau=1.175$ (figure 8(C)), and there is a general convergence of time-varying C_D at the same time (figure 5), it can be inferred that by bristled wings will continue to behave similarly to solid wings throughout the rest of the downstroke, as was indicated by Sunada *et al* (2002) and Lee and Kim (2017).

Chordwise flow fields for one time point each during clap and fling is shown for varying Re (figure 9). During clap, we looked at flow field at $\tau = 0.85$, the time at which maximum lift occurs during clap, and during fling at $\tau = 1.1$, when drag is at its maximum. Key changes are seen to occur in the structure of the leading edge vortices as Re increases (figure 9). At Re = 10, the LEV and TEV remain attached to both wing models during clap, but as Re is increased, the LEVs elongate and shed from the solid wing, as was predicted in Arora *et al* (2014). This is illustrated at Re = 120, where for the bristled wing, the circular flow pattern is behind the wing, rather than attached to the leading edge (figure 9(B)), and for the solid wing, where the circular flow pattern is shed completely from the wing (figure 9(A)). This shed LEV is associated with the loss of lift during clap with increasing Reynolds number (figure 6(B)). TEVs are elongated in both the solid wing and the bristled wing model, and wing wake velocity increases as Re increases. During fling velocity increases with increasing Re, but the vortex core is actually larger at lower Re (figures 9(C) and (D)).

Mid-span circulation at Re = 10

For all wing models at Re = 10, circulation during clap is seen to increase initially until $\tau = 0.85$, and then decrease to zero at $\tau = 1.0$ (figure 10(A)). The time

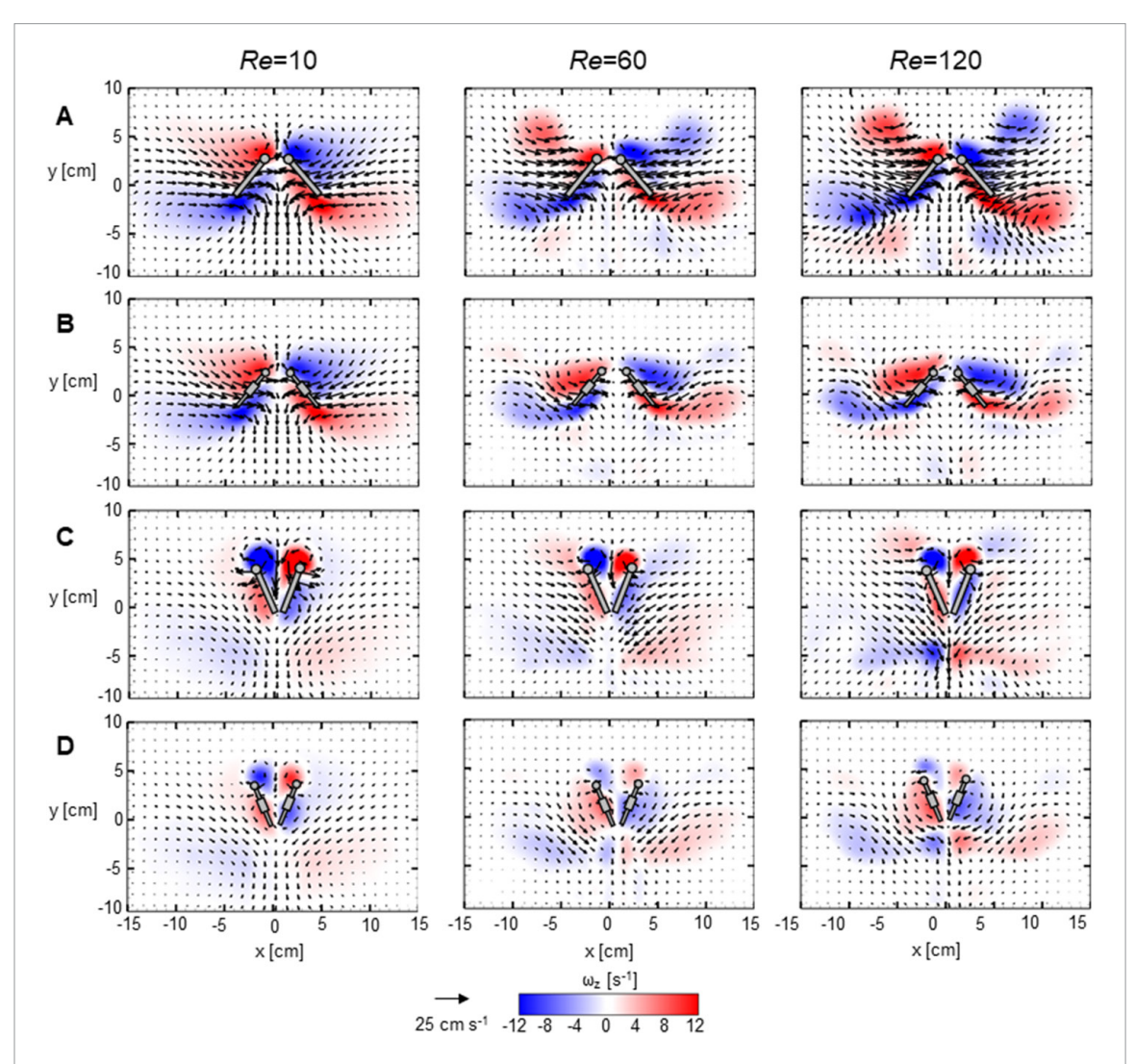


Figure 9. Velocity vector fields overlaid with out-of-plane (z) vorticity contours in the chordwise plane at z/S=0.5 for varying Reynolds number (Re). Figures (A) and (B) correspond to $\tau=0.85$ (25% clap) for the solid wing model (in (A)) and $A_{\rm M}/A_{\rm T}=15\%$ wing model (in (B)). Figures (C) and (D) correspond to $\tau=1.1$ (50% fling) for the solid wing model (in (C)) and $A_{\rm M}/A_{\rm T}=15\%$ wing model (in (D)). The wing position has been superimposed on each image, with the leading edge of each wing represented by a filled circle. Significant changes occur in the flow structures as Reynolds number increases from Re = 10 to Re = 120. Shed leading edge vortices during clap at Re = 60 and Re = 120 can increase vertical asymmetry and thereby increase lift (Miller and Peskin 2005). During fling for Re = 60 and Re = 120, leading edge circulation is greatly reduced for bristled wings with increasing trailing edge circulation, detrimental for lift production.

point at which peak circulation occurs, $\tau = 0.85$, is also the time point at which the peak lift coefficient is found to occur (figures 5(D) and 10(A)). Viscous dissipation as the wings come to a stop at $\tau = 1.0$ results in the circulation reaching zero magnitude at the end of clap, and prevents the LEV and TEV from clap from interacting with the counter-rotating vortices formed during the fling. The maximum values of circulation are found to be larger in clap than in fling (figures 10(A) and (C)), which agrees with the force results for Re = 10 (compare figures 6(B) and (E)). Circulation in both the LEV and TEV was found to decrease slightly with decreasing $A_{\rm M}/A_{\rm T}$ during clap (figure 10(A)), which is in agreement with the force data, and to decrease more substantially during fling. The velocity vector fields (figures 7 and 8) show that bristles help to diffuse the vortices on the side of the wing opposite the axis of rotation (LE in clap, TE in fling), which results in increased vortical asymmetry in clap (figure 10(A)),

but decreased asymmetry in fling (figure 10(C)). The result of increased asymmetry, coupled with decreased horizontal velocity (figure 7(C)) causes wings with lower $A_{\rm M}/A_{\rm T}$ to have higher lift to drag ratios during clap at Re = 10 (figure 6(C)).

Effect of increasing Re on mid-span circulation

Decreasing $A_{\rm M}/A_{\rm T}$ was generally found to decrease circulation at Re = 60 and Re = 120 as well as at Re = 10. However, shedding of the LEV (and the subsequent development of a weaker attached LEV) during the upstroke results in lower bound LEV circulation for wings with high $A_{\rm M}/A_{\rm T}$ at the start of clap (τ = 0.8–0.85), and increasing $A_{\rm M}/A_{\rm T}$ resulted in decreasing circulation in the LEV (figure 10(B)). This LEV shedding was also seen in a previous computational study using only solid wings (Arora *et al* 2014). At τ = 0.85 wing translation slows, and the previously shed LEV merges with the

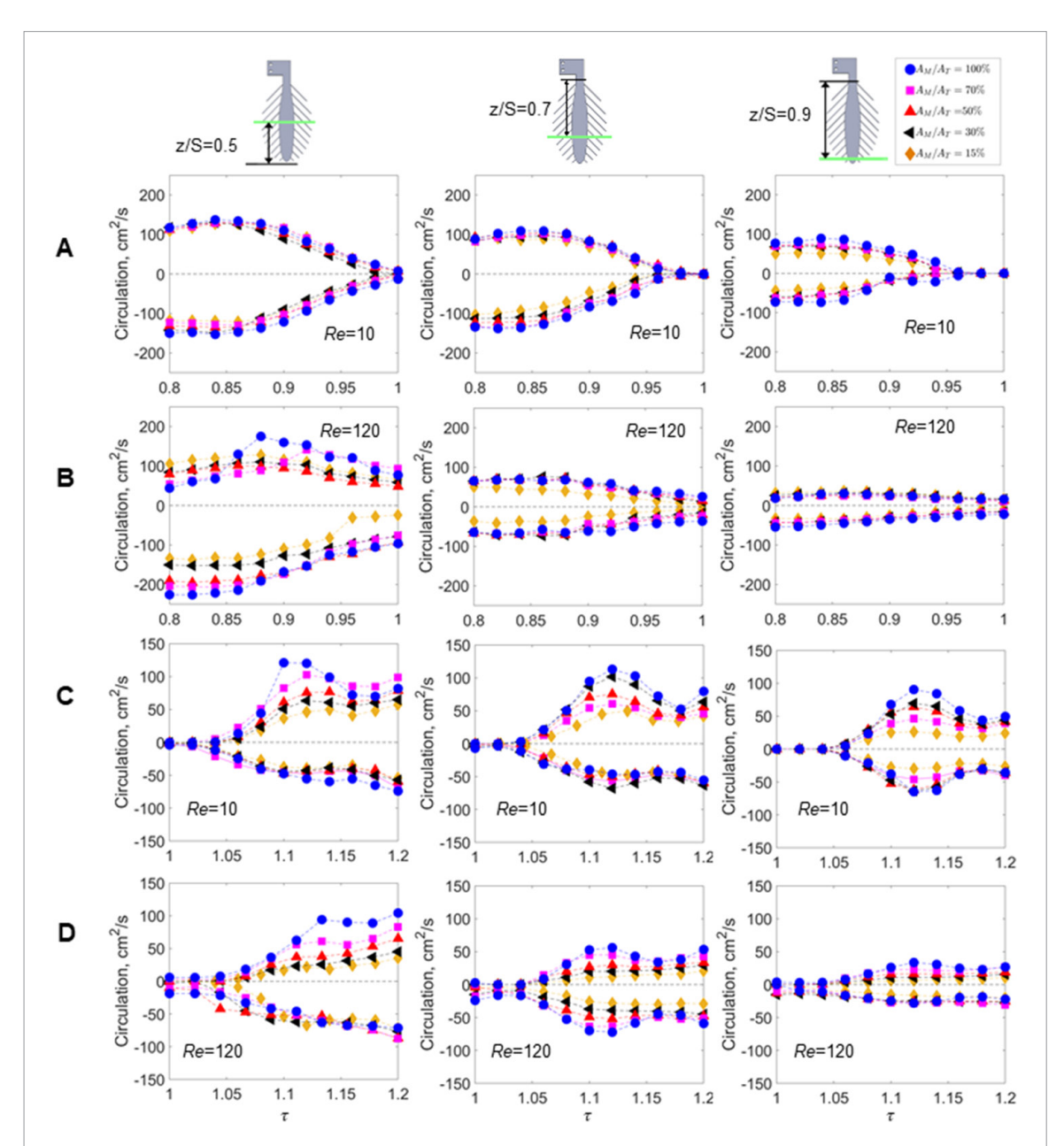


Figure 10. LEV and TEV circulation during clap and fling. Figures (A) and (B) represent circulation during clap at Re = 10 and Re = 120; (C) and (D) represent circulation during fling. For both clap and fling, positive values correspond to LEV circulation and negative values correspond to TEV circulation. Columns from left to right represent the chordwise planes at z/S = 0.5, z/S = 0.7, and z/S = 0.9, respectively. Circulation magnitude is seen to decrease along the span of the wing, especially at higher Re. Asymmetry between circulation in the leading and trailing edge vortices contributes to lift generation (Miller and Peskin 2005). Elongation and shedding of the LEV during clap at Re = 120 (B) results in wings with higher A_M/A_T having lower LEV circulation initially, until the motion slows enough for the shed vortex to reattach at approximately $\tau = 0.85$.

attached LEV at $\tau\approx 0.88$. This results in increasing $\Gamma_{\rm LEV}$ for: 1) solid wing at Re = 60, and 2) both the solid and $A_{\rm M}/A_{\rm T}=70\%$ wings at Re = 120. After reattachment of the previously shed LEV, the wing with $A_{\rm M}/A_{\rm T}=70\%$ again shows higher $\Gamma_{\rm LEV}$ than the solid wing at Re = 120. Unlike at Re = 10, the TEV from clap does not immediately dissipate, but attaches to the trailing edge of the bristled wing models at the beginning of the fling, increasing TEV circulation and symmetry in the bristled wing models compared to the solid wing model. Unlike at Re = 10, circulation in the LEV continues to increase throughout the fling at Re = 120, which is likely due to the fact that it is easier to generate circulation through pure translation

at higher Re than at low Re. At Re = 60 (figure S2 part B) and Re = 120 (figure 10(D)), the circulation magnitude continues to increase though the end of fling, which is when the maximum lift coefficients occur for Re = 60 (figure 5(B)) and Re = 120 (figure 5(C)).

Regardless of Re, magnitudes of TEV circulation (negative values in figures 10(A) and (B)) are larger than magnitudes of LEV circulation during clap (positive values in figures 10(A) and (B)), while magnitudes of LEV circulation (positive values in figures 10(C) and (D)) are larger than those of TEV circulation (negative values in figures 10(C) and (D)) during fling. This vortical asymmetry has been proposed to con-

tribute to lift generation (Wu 1981, Miller and Peskin 2005). In general, all wing models showed greater asymmetry in circulation during clap at Re > 10 than at Re = 10, which does not agree with the finding of greater lift coefficients in clap at lower Re. Due to this disagreement with the force results, we hypothesized that chordwise flow at locations farther along the span would not show the same trends with changing Re as chordwise flow in the mid-span plane.

Spanwise decay of LEV-TEV circulation with increasing Reynolds number

During clap at both Re = 10 (figure 10(A)) and Re = 120 (figure 10(B)), the magnitude of circulation at the mid-span of the wing in both the LEV and TEV is reduced as wing motion slowed down. However, due to viscous dissipation at Re = 10, the mid-span circulation is reduced to zero at the end of clap (figure 10(A)). For both Re = 60 (figure S2 part S3) and S40 (figure S41), mid-span circulation at the end of clap did not diminish close to zero.

Along the span, LEV and TEV circulation during clap are largely maintained at Re = 10 (figure 10(A)), especially when compared with Re = 60 (figure S2) part A) and Re = 120 (figure 10(B)). At Re = 60, circulation at the end of clap is not reduced to zero at 50% and 70% span, but is reduced close to zero at 90% span (figure S2 part A). Similarly at Re = 120, circulation at the end of clap is also reduced with moving from 50% span to 70% span, and is nearly zero at 90% span (figure 10(B)). As in clap, circulation is maintained during fling along the length of the span at Re = 10, but not at Re = 120. A rapid rise in circulation magnitude occurs during the first half of the fling ($\tau = 1.0$ to 1.1) at Re = 10 (figure 10(C)), and then circulation starts to fall and level off with further progression of fling. This pattern of time variation of circulation of LEV and TEV in fling is essentially unaffected when moving to 70% span and 90% span locations at Re = 10 (figure 10(C)). Similar to clap, circulation of LEV and TEV in fling decays with increasing span location for Re = 60(figure S2 part B) and Re = 120 (figure 10(D)).

Since the motion profiles are identical for each Reynolds number (also unchanged with wing geometry), but the viscosity is changed, the differences in circulation trends can only be due to the change in Re. At Re = 10, vorticity in the LEV and TEV is likely maintained along the span due to large viscous forces causing the fluid to rotate along the 2D chordwise plane. This is supported by the findings of a recent study by Santhanakrishnan *et al* (2018), where no spanwise flow (directed from root to tip of wing) was observed along a single revolving wing at Re on the orders of 1 to 10. Increasing Re would result in lowering viscous forces, which in turn likely permits decay of LEV and TEV circulation from mid-span to wing tip. These differences in LEV and TEV circulation along the span of the wing support the lift reduction observed when increasing Re, from the scale relevant to flapping flight of tiny

insects (Re = 10) to those of fruit flies (Re = 120). This suggests that clap and fling may not be an ideal choice for free-flight kinematics in larger insects.

Conclusions

The ratio of membrane area to total area ($A_{\rm M}/A_{\rm T}$) was examined in the forewings of 25 species of thrips, and a positive correlation was found between $A_{\rm M}/A_{\rm T}$ and body length. $A_{\rm M}/A_{\rm T}$ for all species of thrips considered in this study was found to fall in a narrow range of 14%–27%.

At the Reynolds number relevant to tiny insects, bristled wings generated lift similar to solid wings, but generated substantially less drag. Bristled wings with $A_{\rm M}/A_{\rm T}$ in the range of thrips forewings (15%–30%) generated the largest lift to drag ratios in clap and fling at Re = 10, relevant to the flapping flight of tiny insects.

As Re increased by an order of magnitude from 10 to 120, bristled wings still performed better in terms of lift to drag ratio than solid wings in clap and fling. However, less lift was generated at Re=120 on account of circulation of the LEV and TEV decaying along the span, rendering the use of clap and fling less beneficial for larger insects such as fruit flies.

Acknowledgments

The authors would like to thank the members of the Applied Fluid Mechanics Lab at Oklahoma State University for feedback on the manuscript, and two anonymous reviewers for their constructive comments.

Competing interests

The authors declare no financial or otherwise competing interests.

Funding

This research was funded by the National Science Foundation (CBET 1512071 to AS), and by the Lew Wentz Foundation at Oklahoma State University (Wentz Research Grant to MPF).

ORCID iDs

Arvind Santhanakrishnan https://orcid.org/0000-0003-1800-8361

References

Arora N, Gupta A, Sanghi S, Aono H and Shyy W 2014 Lift-drag and flow structures associated with the 'clap and fling' motion *Phys. Fluids* **26** 071906

Austin A and Dowton M 2000 Hymenoptera: Evolution, Biodiversity and Biological Control (Collingwood: Csiro Publishing)

- Bennett L 1977 Clap and fling aerodynamics, an experimental evaluation *J. Exp. Biol.* **69** 261–72
- Cavalleri A and Mound L 2012 Toward the identification of Frankliniella species in Brazil (Thysanoptera, Thripidae) Zootaxa 3270 1–30
- Cheer A and Koehl M 1987 Paddles and rakes: fluid flow through bristled appendages of small organisms *J. Theor. Biol.* 129 17–39
- de Borbón C M 2010 The Heterothrips species of Argentina, with two new species and biological notes (Thysanoptera, Heterothripidae) Zootaxa 2562 45–56
- Ellington C P 1984 The aerodynamics of hovering insect flight: III. Kinematics *Phil. Trans. R. Soc. Lond.* B 305 41–78
- Ellington C P, van den Berg C, Willmont A P and Thomas A L R 1996 Leading edge vortices in insect flight *Nature* 348 626–30
- Funderburk J, Diffie S, Sharma J, Hodges A and Osborne L 2007
 Thrips of ornamentals in the Southeastern US *Technical Report*ENY-845 (IN754) (University of Florida Institute of Food and
 Agricultural Sciences) (http://ipm.ifas.ufl.edu/pdfs/IN75400.
 pdf)
- Harbig R R, Sheridan J and Thompson M C 2013 Reynolds number and aspect ratio effects on the leading-edge vortex for rotating insect wing planforms J. Fluid Mech. 717 166–92
- Jones D R 2005 Plant viruses transmitted by thrips Eur. J. Plant Pathol. 113 119–57
- Jones S, Yun Y, Hedrick T, Griffith B and Miller L 2016 Bristles reduce the force required to 'fling' wings apart in the smallest insects *J. Exp. Biol.* **219** 3759–72
- Kasoju V T, Terrill C, Ford M and Santhanakrishnan A 2018 Leaky flow through simplified physical models of bristled wings of tiny insects during clap and fling *Fluids* 3 44
- Kolomenskiy D, Moffatt H K, Farge M and Schneider K 2011 The Lighthill–Weis–Fogh clap-fling-sweep mechanism revisited J. Fluid Mech. 676 572–606
- Lee S and Kim D 2017 Aerodynamics of a translating comb-like plate inspired by a fairyfly wing *Phys. Fluids* 29 081902
- Lehmann F O, Sane S P and Dickinson M 2005 The aerodynamic effects of wing–wing interaction in flapping insect wings J. Exp. Biol. 208 3075–92
- Lighthill M J 1973 On the Weis–Fogh mechanism of lift generation J. Fluid Mech. $60\,1-17$
- Lima E F B and Mound L 2016 Species-richness in neotropical Sericothripinae (Thysanoptera: Thripidae) *Zootaxa* 4162 001–45
- Lin N, Huber J T and La Salle J 2007 The Australian genera of Mymaridae (Hymenoptera: Chalcidoidea) *Zootaxa* **1596** 1–111
- Maxworthy T 1979 Experiments on the Weis–Fogh mechanism of lift generation by insects in hovering flight. Part 1: Dynamics of the 'fling' *J. Fluid Mech.* **93** 47–63

- Miller L and Peskin C 2004 When vortices stick: an aerodynamic transition in tiny insect flight *J. Exp. Biol.* **207** 3073–88
- Miller L and Peskin C 2005 A computational fluid dynamics of 'clap and fling' in the smallest insects *J. Exp. Biol.* **208** 195–212
- Miller L and Peskin C 2009 Flexible clap and fling in tiny insect flight J. Exp. Biol. 212 3076–90
- Minaei K and Aleosfoor M 2013 A new species of *Haplothrips* from southern Iran (Thysanoptera Phlaeothripidae) *Zookeys* 275 91–9
- Morse J and Hoddle M 2006 Invasion biology of thrips *Annu. Rev. Entomol.* **51** 67–89
- Mound L 2005 Thysan optera: diversity and interactions Annu. Rev. Entomol. 50 247-69
- Mound L and Ng Y F 2009 An illustrated key to the genera of Thripinae (Thysanoptera) from south east Asia *Zootaxa* **2265** 27–47
- Polilov A 2015 Small is beautiful: features of the smallest insects and limits to miniaturization *Annu. Rev. Entomol.* **60** 103–21
- Riley D, Joseph S, Srinivasan R and Diffie S 2011 Thrips vectors of tospoviruses *J. Integr. Pest Manage*. 2 1–10
- Sane S P 2016 Neurobiology and biomechanics of flight in miniature insects Curr. Opin. Neurobiol. 41 158–66
- Santhanakrishnan A, Jones S, Dickson W, Peek M, Kasoju V, Dickinson M and Miller L 2018 Flow structure and force generation on flapping wings at low Reynolds numbers relevant to the flight of tiny insects *Fluids* 3 45
- Santhanakrishnan A, Robinson A, Jones S, Low A A, Gadi S, Hedrick T and Miller L 2014 Clap and fling mechanism with interacting porous wings in tiny insect flight *J. Exp. Biol.* 217 3898–909
- Schneider C, Rasband W and Eliceiri K 2012 NIH Image to ImageJ: 25 years of image analysis *Nat. Methods* **9** 671–5
- Sunada S, Takashima H, Hattori T, Yasuda K and Kawachi K 2002 Fluid-dynamic characteristics of a bristled wing *J. Exp. Biol.* **205** 2737–44
- Tong X, Wang Z and Zhao C 2015 Remarkable sexually dimorphic *Aroidothrips longistylus* newly recorded from China (Thysanoptera: Thripidae) *Zootaxa* **4028** 148–50
- Ullman D E, Meideros R, Campbell L R, Whitfield A E, Sherwood J L and German T L 2002 Thrips as vectors of tospoviruses *Adv. Bot. Res.* 36 113–40
- Weis-Fogh T 1973 Quick estimates of flight fitness in hovering animals, including novel mechanisms for lift production *J. Exp. Biol.* **59** 169–230
- Wu J C 1981 Theory for aerodynamic force and moment in viscous flows AIAA J. $19\,432-41$